

UC Berkeley

UC Berkeley Previously Published Works

Title

Network design for quantifying urban CO₂ emissions: assessing trade-offs between precision and network density

Permalink

<https://escholarship.org/uc/item/8j46c4m6>

Journal

Atmospheric Chemistry and Physics, 16(21)

ISSN

1680-7316

Authors

Turner, Alexander J
Shusterman, Alexis A
McDonald, Brian C
[et al.](#)

Publication Date

2016

DOI

10.5194/acp-16-13465-2016

Peer reviewed



Network design for quantifying urban CO₂ emissions: assessing trade-offs between precision and network density

Alexander J. Turner^{1,2}, Alexis A. Shusterman³, Brian C. McDonald^{4,a}, Virginia Teige³, Robert A. Harley⁴, and Ronald C. Cohen^{3,5}

¹School of Engineering and Applied Sciences, Harvard University, Cambridge, Massachusetts, USA

²Environmental Energy and Technologies Division, Lawrence Berkeley National Laboratory, Berkeley, CA, USA

³Department of Chemistry, University of California at Berkeley, Berkeley, CA, USA

⁴Department of Civil and Engineering, University of California at Berkeley, Berkeley, CA, USA

⁵Department of Earth and Planetary Sciences, University of California at Berkeley, Berkeley, CA, USA

^anow at: Cooperative Institute for Research in Environmental Sciences, University of Colorado Boulder, Boulder, Colorado, USA

Correspondence to: Ronald C. Cohen (rccohen@berkeley.edu)

Received: 25 April 2016 – Published in Atmos. Chem. Phys. Discuss.: 24 May 2016

Revised: 7 October 2016 – Accepted: 13 October 2016 – Published: 1 November 2016

Abstract. The majority of anthropogenic CO₂ emissions are attributable to urban areas. While the emissions from urban electricity generation often occur in locations remote from consumption, many of the other emissions occur within the city limits. Evaluating the effectiveness of strategies for controlling these emissions depends on our ability to observe urban CO₂ emissions and attribute them to specific activities. Cost-effective strategies for doing so have yet to be described. Here we characterize the ability of a prototype measurement network, modeled after the Berkeley Atmospheric CO₂ Observation Network (BEACO₂N) in California's Bay Area, in combination with an inverse model based on the coupled Weather Research and Forecasting/Stochastic Time-Inverted Lagrangian Transport (WRF-STILT) to improve our understanding of urban emissions. The pseudo-measurement network includes 34 sites at roughly 2 km spacing covering an area of roughly 400 km². The model uses an hourly 1 × 1 km² emission inventory and 1 × 1 km² meteorological calculations. We perform an ensemble of Bayesian atmospheric inversions to sample the combined effects of uncertainties of the pseudo-measurements and the model. We vary the estimates of the combined uncertainty of the pseudo-observations and model over a range of 20 to 0.005 ppm and vary the number of sites from 1 to 34. We use these inversions to develop statistical models that estimate the efficacy of the combined model–observing system in reducing uncertainty

in CO₂ emissions. We examine uncertainty in estimated CO₂ fluxes on the urban scale, as well as for sources embedded within the city such as a line source (e.g., a highway) or a point source (e.g., emissions from the stacks of small industrial facilities). Using our inversion framework, we find that a dense network with moderate precision is the preferred setup for estimating area, line, and point sources from a combined uncertainty and cost perspective. The dense network considered here (modeled after the BEACO₂N network with an assumed mismatch error of 1 ppm at an hourly temporal resolution) could estimate weekly CO₂ emissions from an urban region with less than 5 % error, given our characterization of the combined observation and model uncertainty.

1 Introduction

Carbon dioxide (CO₂) is an atmospheric trace gas and the single largest anthropogenic radiative forcer, with a radiative forcing of 1.82 W m⁻² in 2011 relative to preindustrial times (IPCC, 2013). CO₂ has increased from 280 ppm in preindustrial times to greater than 400 ppm in the present, largely due to changes in fossil fuel emissions. Over 70 % of these fossil fuel CO₂ emissions in the United States (US) are attributable to urban areas (US EIA, 2015; Hutyra et al., 2014), yet current bottom–up inventories still have large un-

certainties. For this reason, quantifying and monitoring the emissions from urban areas is crucial to strategies for reducing future increases in CO₂.

Numerous studies have performed top-down estimations of CO₂ emissions using observations from urban surface monitoring networks of various sizes (e.g., Gratani and Varone, 2005; McKain et al., 2012; Newman et al., 2013; Lauvaux et al., 2013; Bréon et al., 2015; Turnbull et al., 2015). However, it is not immediately clear how many sites are necessary to monitor the emissions from an urban area. Kort et al. (2013) found that a surface monitoring network would need at least eight sites operating for 8 weeks to accurately estimate CO₂ emissions in Los Angeles. Yet most current urban monitoring networks have fewer than eight sites but operate for much longer than 8 weeks. For example, Gratani and Varone (2005) used a single site in Rome, Newman et al. (2013) used a single site in Los Angeles, Lauvaux et al. (2013) used two sites in Davos, Switzerland, McKain et al. (2012) used a network of five sites in Salt Lake City, and Bréon et al. (2015) used five sites in Paris. Recent work from Turnbull et al. (2015) employed a denser network of 12 sites in Indianapolis.

This issue is further complicated by bias and noise in both the measurements and the modeling framework. The combined model and measurement error is known as the model-data mismatch error (hereafter referred to as the “mismatch error”). Current monitoring networks use a mix of instruments and approaches to calibration with resulting variations of capital and operating costs, network precision, and potential instrument bias. Monitoring networks located in regions with complex orography are challenging for atmospheric transport calculations, making it more difficult to determine the dispersion from sources.

The trade-off between measurement network density and mismatch error has yet to be characterized. Understanding these trade-offs is crucial to reducing the uncertainty in emissions from urban regions and to developing cost-effective urban monitoring networks. Here we present a high-resolution inventory of CO₂ fluxes and a numerical model that relates atmospheric observations to high-resolution surface fluxes. We then use this inventory and model in a series of observing system simulation experiments (OSSEs) to investigate the trade-off between reductions in the mismatch error and increases in the measurement network density. We develop statistical models to characterize this relationship for different types of sources in the San Francisco (SF) Bay Area, identify limiting regimes, and recommend future observing strategies.

2 Constructing a high-resolution regional CO₂ inventory

McDonald et al. (2014) demonstrated that $1 \times 1 \text{ km}^2$ spatial resolution is necessary to resolve the gradients in ur-

ban CO₂ fluxes from highways. However, most of the existing CO₂ anthropogenic inventories are not available at this resolution. For example, the Emissions Database for Global Atmospheric Research (EDGAR) (European Commission, 2011) and VULCAN (Gurney et al., 2009) are only available at $0.1^\circ \times 0.1^\circ$ and $10 \times 10 \text{ km}^2$, respectively. A notable exception is the Open-Data Inventory for Anthropogenic Carbon dioxide (ODIAC) fossil fuel CO₂ (Oda and Maksyutov, 2011), which is based on satellite-observed nightlight data and available globally at $1 \times 1 \text{ km}^2$ resolution. High-resolution fossil fuel CO₂ emissions are available for select cities and sectors such as Paris through the AirParif inventory (Bréon et al., 2015; <http://www.airparif.asso.fr/en/index/index>) and Indianapolis, Los Angeles, Salt Lake City, and Phoenix through the Hestia project (Gurney et al., 2012; <http://hestia.project.asu.edu/>); three recent studies (Gately et al., 2013; McDonald et al., 2014; Gately et al., 2015) developed high-resolution CO₂ emissions from vehicular traffic.

The Bay Area Air Quality Management District (BAAQMD) provides detailed annual county-level CO₂ emissions information for San Francisco and California's Bay Area (Mangat et al., 2010). The BAAQMD found that the transportation sector accounted for 36% of the Bay Area anthropogenic emissions, industrial and commercial for 36%, electricity for 16%, residential fuel usage for 7%, off-road equipment for 3%, and agriculture for 1%. The BAAQMD also reports CO₂ emissions for 4375 point sources in the Bay Area. We geocode these point sources based on the addresses provided by the BAAQMD. These point sources capture the emissions from the industrial, commercial, and electricity sectors. We map residential fuel usage to population using block level population data from the 2010 US Census and apply a temporal temperature scaling based on Deschênes and Greenstone (2011); the resulting temporal scaling effect is small due to the temperate climate in the East Bay region of the SF Bay Area.

Here we use the traffic CO₂ emissions from the fuel-based inventory for vehicle emissions (FIVE) developed by McDonald et al. (2014). The FIVE traffic CO₂ inventory provides a representative week of hourly CO₂ emissions for San Francisco and other nearby Bay Area cities at 10, 4, 1 km, and 500 m resolution. This representative week can be scaled to different years based on the state fuel sales (see McDonald et al., 2014, for additional details). The FIVE inventory is constructed by partitioning CO₂ emissions using state-level fuel data to individual roads with road-specific traffic count data and temporal patterns from weigh-in-motion data. In this manner, CO₂ emissions from the FIVE inventory will be consistent with state and national CO₂ budgets and can easily be scaled to different years.

Combining the industrial, commercial, electricity, residential, and traffic emissions account for 95.8% of the anthropogenic CO₂ emissions in the Bay Area. We do not have high-resolution proxy data for the off-road equipment or agriculture sectors in the Bay Area and have chosen to as-

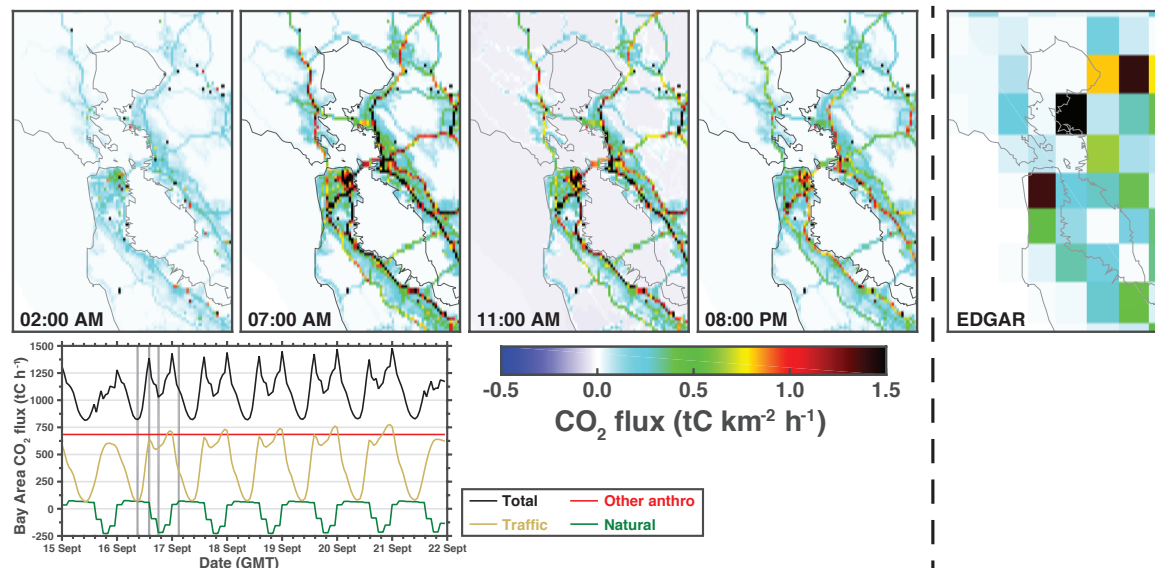


Figure 1. September 2013 CO₂ fluxes from bottom-up inventories. Top row shows the fluxes in the Bay Area (122.0357–122.7683° W, 37.3771–38.2218° N) at four representative hours (hour in local time). Right panel shows the atemporal EDGAR v4.2 FT2010 CO₂ flux in the Bay Area. Bottom panel shows the total Bay Area CO₂ flux (black), traffic (orange), other anthropogenic (red), and natural (green) sources. Vertical gray shading indicates the time slices plotted in the top and middle panels.

sume their contributions are smaller than the uncertainty in the total budget; therefore, we neglect these sectors in the construction of our inventory.

CarbonTracker CT2013B (<http://www.esrl.noaa.gov/gmd/ccgg/carbontracker/>; Peters et al., 2007) provides 3-hourly fossil fuel, ocean, biogenic, and fire CO₂ fluxes at 1° × 1° resolution. These fluxes are optimized to agree with atmospheric CO₂ observations. We regrid these fluxes to 1 × 1 km² spatial resolution (see Supplement Sect. S3) and use the fire, ocean, and biogenic sectors to account for our natural fluxes.

Figure 1 shows snapshots of the CO₂ fluxes from our inventory at four different times of day and the atemporal fluxes from EDGAR v4.2 FT2010 (European Commission, 2011). From Fig. 1 we can see that the inventory clearly resolves the large CO₂ gradients from highways, confirming that 1 × 1 km² spatial resolution is sufficient to resolve urban CO₂ fluxes from highways. The bottom panel of Fig. 1 shows a time series of Bay Area CO₂ fluxes broken down by source. The diurnal cycle in our inventory is largely driven by the traffic emissions with modest uptake from the biosphere during the middle of the day. Other anthropogenic sources were assumed to have a negligible diurnal cycle (Nassar et al., 2013). In what follows, we use EDGAR as the prior and the high spatio-temporal resolution inventory as the “truth”.

3 The Berkeley Atmospheric CO₂ Observation Network (BEACO₂N)

The Berkeley Atmospheric CO₂ Observation Network (BEACO₂N; see <http://beacon.berkeley.edu> and Shusterman et al., 2016) was founded in 2012 as a web of approximately 25 carbon dioxide sensing “nodes” stationed atop schools and museums in the Oakland, CA, metropolitan area (see Table 1). With sensors installed on an approximately 2 km square grid, BEACO₂N is the only surface-level (3 to 130 m a.g.l.) greenhouse gas monitoring system with roughly the same spatial resolution as the emissions inventories described above. Each node requires only a standard, 120 V power source and is sited on preexisting structures based on voluntary, no-cost partnerships. The BEACO₂N configuration therefore represents a reasonable expectation and is one model for future monitoring networks aimed at constraining CO₂ fluxes on neighborhood scales within an urban dome.

BEACO₂N’s unprecedented spatial density is achieved by exploiting lower-cost instrumentation than has traditionally been utilized for ambient CO₂ detection. The nondispersive infrared (NDIR) absorption sensor used in each BEACO₂N node (<http://www.vaisala.com/en/products/carbondioxide/Pages/GMP343.aspx>) has been seen to possess adequate sensitivity to resolve diurnal as well as seasonal phenomena relevant to urban environments (Rigby et al., 2008) and costs 1 to 2 orders of magnitude less than the commercial cavity ring-down instruments commonly used in other networks. However, the low-cost NDIR sensor is more susceptible to factors such as temporal drift and environmen-

Table 1. The 34 sites in the network* used in this study.

Site code	Site name	Latitude (°N)	Longitude (°W)	Height (m a.g.l.)
AHS	Arroyo High School	37.680	122.139	3
BEL	Burckhalter Elementary School	37.775	122.167	5
BFE	Bayfarm Elementary School	37.744	122.251	3
BOD	Bishop O'Dowd High School	37.753	122.155	3
CES	Claremont Elementary School	37.846	122.252	3
CHA	Chabot Space & Science Center (low)	37.819	122.181	3
CHB	Chabot Space & Science Center (high)	37.819	122.181	9
COI	Coit Tower	37.8030	122.406	5
CPS	College Preparatory School	37.849	122.242	24
EBM	W. Oakland EBMUD Monitoring Station	37.814	122.282	3
ELC	El Cerrito High School	37.907	122.294	8
EXB	Exploratorium (Bay)	37.803	122.397	6
EXE	Exploratorium (Embarcadero)	37.801	122.399	3
FTK	Fred T. Korematsu Discovery Academy	37.738	122.174	3
GLE	Greenleaf Elementary School	37.765	122.194	3
HRS	Head Royce School	37.809	122.204	7
ICS	International Community School	37.779	122.231	3
KAI	Kaiser Center	37.809	122.264	127
LAU	Laurel Elementary School	37.792	122.197	12
LBL	Lawrence Berkeley National Lab, Bldg. 70	37.876	122.252	3
LCC	Lighthouse Community Charter School	37.736	122.196	3
MAR	Berkeley Marina	37.863	122.314	3
MON	Montclair Elementary School	37.830	122.212	3
NOC	N. Oakland Community Charter School	37.833	122.277	3
OMC	Oakland Museum of California	37.799	122.264	3
PAP	PLACE at Prescott Elementary	37.809	122.298	3
PDS	Park Day School	37.832	122.257	3
PHS	Piedmont Middle & High School	37.824	122.233	3
POR	Port of Oakland Headquarters	37.796	122.280	3
OHS	Oakland High School	37.805	122.236	3
ROS	Rosa Parks Elementary School	37.865	122.295	3
SHA	Skyline High School (low)	37.798	122.162	3
SHB	Skyline High School (high)	37.798	122.162	13
STL	St. Elizabeth High School	37.779	122.222	3

* This study uses both operational and proposed sites. See Shusterman et al. (2016) and <http://beacon.berkeley.edu/> for more information on the network.

tal instability that can negatively impact data quality. This trade-off between mismatch error and network density is explored below.

4 Observing system simulation experiments

CO₂ concentrations were simulated at 34 sites in the BEACO₂N network with the Stochastic Time-Inverted Lagrangian Transport (STILT) model (Lin et al., 2003), coupled to the Weather Research and Forecasting (WRF) mesoscale meteorological model run at 1 × 1 km² grid resolution (WRF-STILT; Nehrkorn et al., 2010). WRF-STILT computes footprints (Δ CO₂ per surface flux, or ppm per μmol m⁻² s⁻¹; see Supplement Sect. S1 and Lin et al. (2003) for additional details) for each observation that relate the

hourly 1 km² CO₂ fluxes (\mathbf{x} ; an $m \times 1$ vector) to the observations (\mathbf{y} ; an $n \times 1$ vector):

$$\mathbf{y} = \mathbf{H}\mathbf{x}. \quad (1)$$

Each row of the $n \times m$ Jacobian matrix ($\mathbf{H} = \partial \mathbf{y} / \partial \mathbf{x}$) is a reshaped footprint. Figure 2 shows the location of the sites and the average network footprint for 15 to 22 September. The spatial extent of the footprints found here is similar to those found in Bastien et al. (2015), who performed an adjoint-based sensitivity analysis of urban air pollution in the San Francisco Bay area (see their Fig. 2).

Our aim is to estimate hourly CO₂ fluxes at 1 km² over a 1-week period. For this reason, the model domain is 88 km × 101 km, and we solve for 240 h of fluxes (1 week plus 3 additional days of back trajectories). The resulting

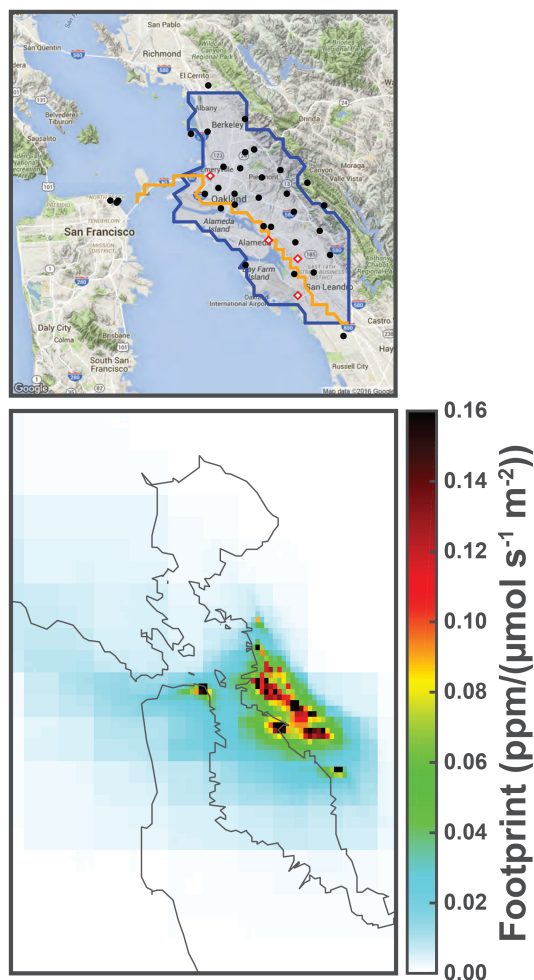


Figure 2. Top panel shows the location of the sites (black circles), the area source (blue region), the line source (orange line), and point sources (red diamonds). Bottom panel shows the 15 to 22 September average footprint for the 34 sites in the network; see Table 1 for a list of the sites. The bottom panel is the full domain used for the inversion. Supplement Fig. S3 shows the footprint on a log scale.

state vector has 2 133 120 elements ($m = m_t \cdot m_x \cdot m_y$ with $m_t = 240$, $m_x = 88$, $m_y = 101$) and the posterior fluxes will have hourly temporal resolution and 1 km^2 spatial resolution. The dimension of n will depend on the number of sites in the observational network.

Here we use our high-resolution CO₂ inventory (\mathbf{x}^* ; an $m \times 1$ vector) to generate synthetic observations (\mathbf{y}^* ; an $n \times 1$ vector):

$$\mathbf{y}^* = \mathbf{H}\mathbf{x}^* + \boldsymbol{\varepsilon}, \quad (2)$$

where $\boldsymbol{\varepsilon}$ is an $n \times 1$ vector of normally distributed noise with mean $\boldsymbol{\varepsilon}_b$ and diagonal covariance matrix \mathbf{R} : $\boldsymbol{\varepsilon} \sim \mathcal{N}(\boldsymbol{\varepsilon}_b, \mathbf{R})$. Using a diagonal \mathbf{R} matrix means that we have assumed that our mismatch errors are uncorrelated. Our base case inversion assumes the mean bias is zero: $\boldsymbol{\varepsilon}_b = \mathbf{0}$. We evaluate the sensitivity to this assumption in Sect. 6 and Supplement

Sect. S6.2. These synthetic observations can then be used in a Bayesian inference framework to estimate the optimal CO₂ fluxes (cf. Rodgers, 2000). Assuming the prior and likelihood distributions are Gaussian gives us a closed-form solution for the posterior CO₂ fluxes:

$$\hat{\mathbf{x}} = \mathbf{x}_p + (\mathbf{H}\mathbf{B})^T (\mathbf{H}\mathbf{B}\mathbf{H}^T + \mathbf{R})^{-1} (\mathbf{y}^* - \mathbf{H}\mathbf{x}_p), \quad (3)$$

where \mathbf{x}_p is an $m \times 1$ vector of prior CO₂ fluxes, comprised of a coarse ($10 \times 10 \text{ km}^2$) atemporal EDGAR v4.2 FT2010 anthropogenic CO₂ inventory and natural fluxes from Carbon-Tracker CT2013B, regridded to $1 \times 1 \text{ km}^2$. \mathbf{B} is the $m \times m$ prior error covariance matrix. The prior error covariance matrix can be expressed as a Kroenecker product (cf. Meirink et al., 2008; Singh et al., 2011; Yadav and Michalak, 2013) of temporal and spatial covariance matrices: $\mathbf{B} = \mathbf{D} \otimes \mathbf{E}$, where \mathbf{D} is the temporal covariance matrix and \mathbf{E} is the spatial covariance matrix. The \mathbf{B} matrix has an uncertainty of 100 % at the native resolution and the spatial and temporal covariance matrices are fully populated (see Supplement Sect. S2 for more details).

We do not explicitly represent the individual error terms contributing to the \mathbf{R} matrix (instrument error, model error, and representation error). Instead, we have assumed that the \mathbf{R} matrix is diagonal and can be characterized by a single parameter: the total mismatch error (σ_m ; $\mathbf{R} = \sigma_m^2 \mathbf{I}$), which represents the combined effects of the different error components.

Figure 3 shows an example of the estimated CO₂ fluxes. We can see that the posterior fluxes capture more of the spatial variability in the CO₂ fluxes than the prior fluxes in the region where the network is deployed. We find substantial improvements in the diurnal cycle (see panel d). Previous work has used the posterior covariance matrix ($\mathbf{Q} = (\mathbf{H}^T \mathbf{R}^{-1} \mathbf{H} + \mathbf{B}^{-1})^{-1}$), averaging kernel matrix ($\mathbf{A} = \mathbf{I} - \mathbf{Q}\mathbf{B}^{-1}$), and the degrees of freedom for signal (DOFs = $\text{tr}(\mathbf{A})$) as metrics to evaluate the information content of different observing systems (e.g., Kort et al., 2013; Wu et al., 2016). However, it is computationally infeasible to construct these $m \times m$ matrices for our application as $m > 10^6$, and storing them would require $\sim 36 \text{ Tb}$ of memory (assuming double-precision, dense matrices).

Instead, we evaluate the efficacy of the posterior fluxes by taking the norm of the difference between the posterior fluxes and the true fluxes: $\|\hat{\mathbf{x}} - \mathbf{x}^*\|_2$. We express this as a relative improvement by comparing the norm of the difference between the prior fluxes and the true fluxes:

$$\eta = 1 - \frac{\|\hat{\mathbf{x}} - \mathbf{x}^*\|_2}{\|\mathbf{x}_p - \mathbf{x}^*\|_2}. \quad (4)$$

This error metric, η , was chosen as it has a similar form to the averaging kernel matrix, but it also allows us to directly compare the posterior fluxes to the true fluxes. This

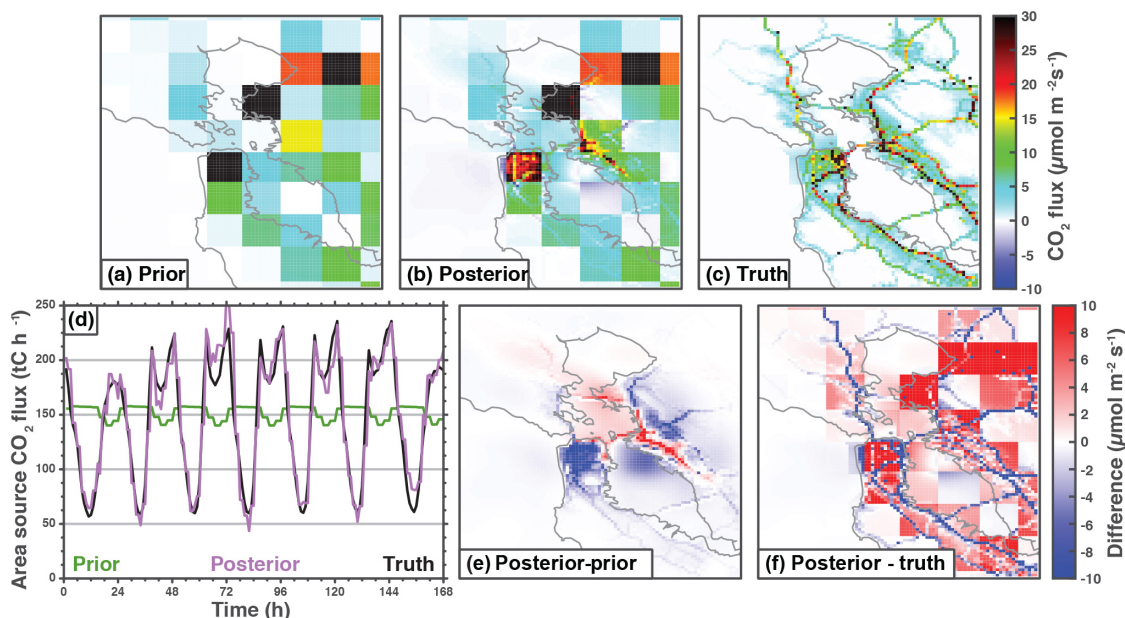


Figure 3. Example of estimated CO₂ fluxes. Top row shows the average emissions from (a) the prior, (b) the posterior, and (c) the true emissions. Panel (d) shows a time series of the emissions from the area source with the prior (green), posterior (pink), and true emissions (black). Panel (e) shows the difference between the posterior and the prior. Panel (f) shows the difference between posterior and the truth. Posterior output is from the best-case scenario ($n_s = 34$ and $\sigma_m = 0.005$ ppm).

relative error metric can be related to the flux error (see Supplement Sect. S5). Therefore, we can use the error metric to evaluate the ability of the observing system to resolve three types of emission sources – (1) area, (2) line, and (3) point sources – by examining a subset of grid cells in the domain (see Sect. S3 for more details). The area source (AS) examined here is the East Bay urban dome (147 ± 55 tC h⁻¹; uncertainty is the 1σ range of hourly fluxes from the high-resolution inventory), the line source (LS) is Interstate 880 and the Bay Bridge (45 ± 20 tC h⁻¹), and the point sources (PS) are 4 large CO₂ sources in the East Bay (9 ± 4 tC h⁻¹). For comparison, Salt Lake City emits $\sim 300 \pm 50$ tC h⁻¹ (McKain et al., 2012). The top panel of Fig. 2 shows these three source types.

Figure 4 shows the error in the estimated CO₂ fluxes using the observations over a wide range of observing system scenarios. We vary the number of sites ($n_s = [1, 2, \dots, 34]$) and the mismatch error ($\sigma_m = [0.005, 0.01, 0.02, 0.05, 0.1, 0.2, 0.5, 1, 2, 5, 10, 20]$ ppm) and perform an ensemble of 20 inversions for each combination to ensure the results are robust. Each ensemble member uses a unique observational network by randomly drawing n_s sites from the population of 34 possible sites. In total, we perform 8160 inversions. Figure 4 shows the mean error in the estimated CO₂ fluxes for the area source, line source, and point source as a function of σ_m and n_s . This figure represents the uncertainty in the estimated emissions at a given hour.

5 Simplified statistical models of error reduction

We develop statistical models to predict the error reduction and quantify the importance of the different factors governing the error reduction. We tested all combinations of models with the following seven parameters (127 possible combinations): $\sqrt{\sigma_m}$, $\sqrt{n_s}$, $\ln(\sigma_m)$, $\ln(n_s)$, σ_m , n_s , and a constant. These statistical models were evaluated using the Akaike information criterion (AIC) and the Bayesian information criterion (BIC). The following statistical models were found to be best:

$$\hat{\eta}_{AS} = \beta_6 \sqrt{\sigma_m} + \beta_5 \sqrt{n_s} + \beta_4 \ln(\sigma_m) + \beta_3 \ln(n_s) + \beta_2 \sigma_m + \beta_0 \quad (5)$$

$$\hat{\eta}_{LS} = \beta_6 \sqrt{\sigma_m} + \beta_5 \sqrt{n_s} + \beta_4 \ln(\sigma_m) + \beta_3 \ln(n_s) + \beta_2 \sigma_m + \beta_1 n_s \quad (6)$$

$$\hat{\eta}_{PS} = \beta_6 \sqrt{\sigma_m} + \beta_5 \sqrt{n_s} + \beta_4 \ln(\sigma_m) + \beta_2 \sigma_m + \beta_0. \quad (7)$$

All the regression coefficients (β_i) in the statistical models yielded statistically significant ($p < 0.001$) parameters based on F tests (see the Supplement Sect. S7 for the regression coefficients and model selection criterion).

We find the $\sqrt{\sigma_m}$, $\sqrt{n_s}$, $\ln(\sigma_m)$, and σ_m parameters in all three statistical models (Eqs. 5–7). This dependence on $\sqrt{n_s}$ and $\sqrt{\sigma_m}$ logically follows from the assumption of Gaussian errors in the derivation of the posterior CO₂ fluxes (Eq. 3) and the basic properties of variance. These two parameters tend to be dominant and generally explain more than 50% of the variance. For this reason, we suspect that these two

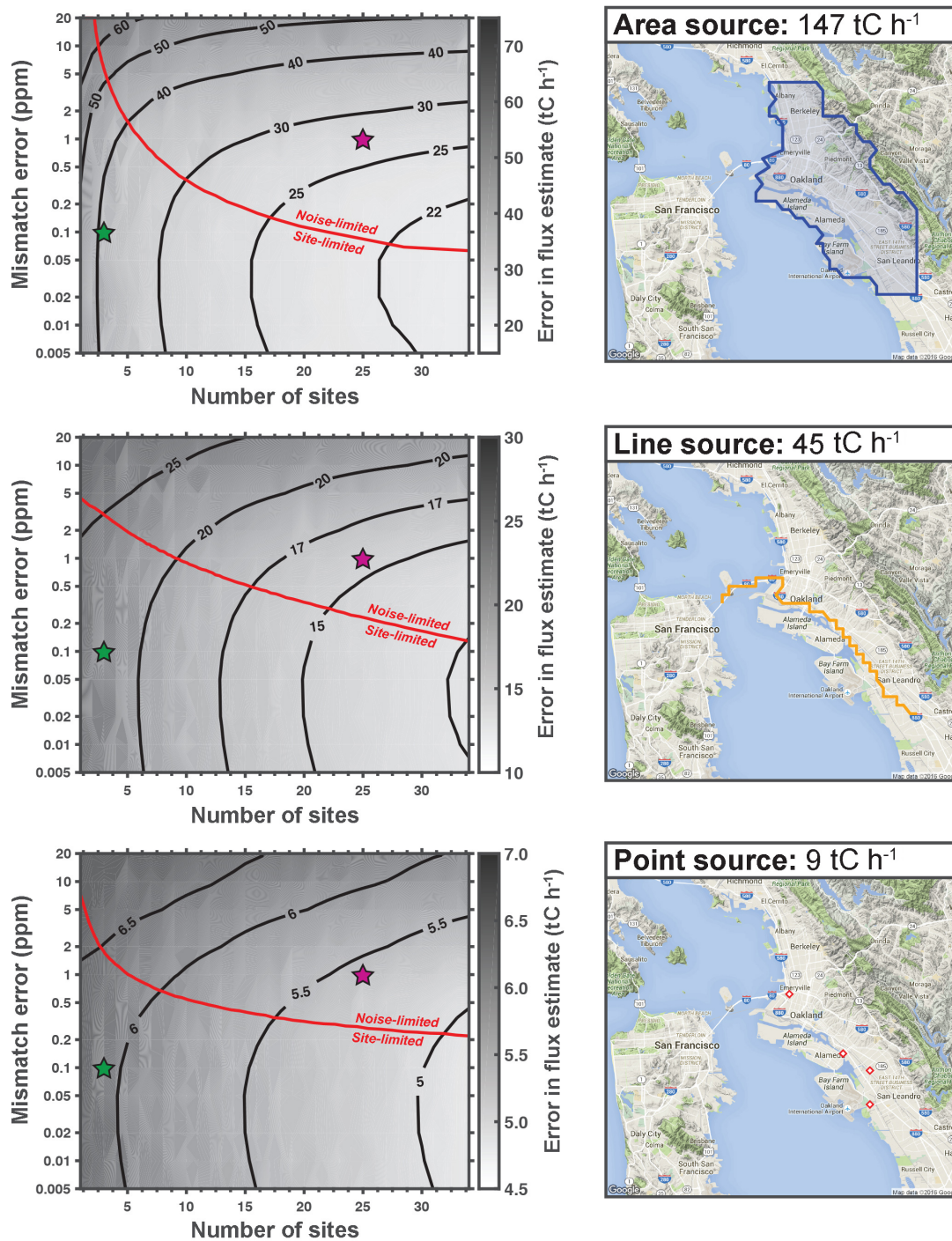


Figure 4. Left column shows the error in the posterior CO₂ fluxes. Right column shows the fluxes being estimated. Top row is the area source, middle row is the line source, and bottom row is the point source. Inversions were performed using $n_s = [1, 2, \dots, 34]$ sites and $\sigma_m = [0.005, 0.01, 0.02, 0.05, 0.1, 0.2, 0.5, 1, 2, 10, 20]$ ppm mismatch error. Results shown are the mean of a Monte Carlo analysis using 20 different combinations of sites for each (n_s, σ_m) pair. Contours are from the statistical models $\hat{\eta}$ (see Eqs. 5–7) converted to flux errors, and the red lines are the ridge lines that define the cutoff between the noise-limited and site-limited regimes. Purple star shows an observing system with 25 sites and 1 ppm noise. Green star shows an observing system with three sites and 0.1 ppm noise. Note the log scale on the y axis.

parameters are the most important and that other terms are capturing higher-order effects.

These statistical models can also be used to define the regimes where increasing the number of sites in the observing system is more important and those where reducing the mismatch error is more important. We estimate these regimes using the ridge line from the statistical models (Eqs. 5–7). From Fig. 4 we can see two distinct regimes: noise-limited and site-limited. Observing systems that lie above the ridge line are in the noise-limited regime where the error reduction is largely governed by the mismatch error in the observing system. Conversely, observing systems below the ridge line are in the site-limited regime where the error reduction is largely governed by the number of sites in the observing system.

The mismatch error is controlled by the instrument, representation, and model error. In the noise-limited regime, reducing these errors will provide the greatest benefit, whereas, in the site-limited regime, the greatest benefit will come from increasing the number of sites in the observing system and there will only be a marginal benefit from reducing the instrument, representation, and model error.

6 Discussion

Three conclusions we can draw from Fig. 4 for California's East Bay are the following:

1. Achieving $\sigma_m = 1$ ppm adds value. There is relatively little additional benefit to reducing mismatch error to 0.1 ppm, particularly for estimating line or point source emissions.
2. At $\sigma_m = 1$ ppm there is a benefit to increasing the number of sites, but this benefit increases more slowly than $\sqrt{n_s}$.
3. At $\sigma_m = 5$ ppm there is little benefit from increasing the number of sites; reducing the noise would add more value.

Our work is primarily focused on estimating hourly fluxes; however, we can further reduce the uncertainty in our estimates by considering temporally averaged fluxes (e.g., what are the weekly or monthly emissions?). Figure 5 shows the error in our estimate of the area source emissions aggregated over various timescales. We find the error in our estimate greatly decreases over the first 72 h. The central limit theorem provides a lower bound on the error reduction we might expect, and the error reductions follow this limit reasonably well over the first 72 h. This implies that our weekly-averaged emission estimate would be 10 times better than our hourly emission estimate.

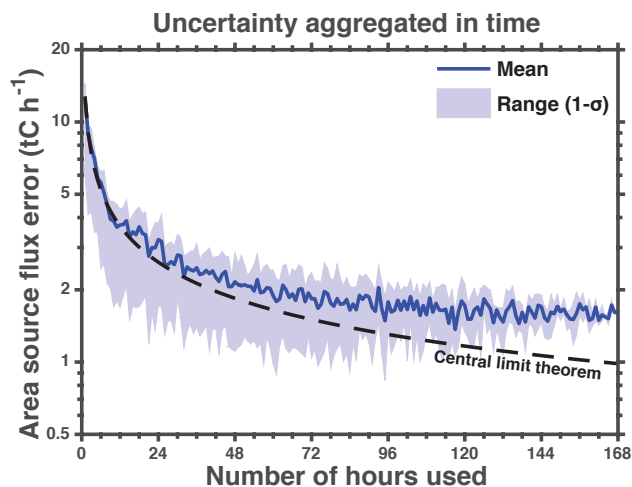


Figure 5. Uncertainty aggregated in time for the best-case inversion (see Fig. 3). The CO₂ flux estimate in this study has an hourly temporal resolution. The uncertainty in the emissions estimate declines as the estimate is averaged to longer temporal scales. Solid blue line is the mean uncertainty, shading is the 1 σ range, and the dashed black line is the uncertainty predicted by the central limit theorem. Note the log scale on the y axis.

6.1 Additional factors affecting observing system design

We considered three additional factors that could adversely impact an observing system: (1) inversion domain size, (2) site-specific systematic biases, and (3) using only day-time observations.

Our results are found to be largely insensitive to the inversion domain size (see Fig. S6). This is discerned through a set of sensitivity OSSEs with a reduced domain size. We find that inversions on the reduced domain were only marginally worse at reducing the error ($\sim 1\%$) than inversions on the full domain (see Supplement Sect. S6.1). This is due to the strong local signal in the footprint of the measurements (see bottom panel of Fig. 2). Therefore, the nonlocal emission sources do not adversely impact our ability to estimate urban emissions.

Biases can adversely impact the observing system (see Fig. S7). To test the impacts of biases in the modeling–measurement framework, we repeated the OSSEs outlined in Sect. 4 but included a systematic bias. The bias was unique to each site and was drawn from a normal distribution ($\epsilon_b \sim \mathcal{N}(\mathbf{0}, \sigma_b^2 \mathbf{I})$; $\sigma_b = 1$ ppm). There are three major findings from the OSSEs with systematic biases:

1. Systematic biases become particularly problematic when the spread of the potential biases (defined here as σ_b) is larger than the mismatch error ($\sigma_b > \sigma_m$). This is because we have defined the observational error covariance matrix as $\mathbf{R} = \sigma_m^2 \mathbf{I}$. However, if $\sigma_b > \sigma_m$ with a dense observing system, then the site-specific biases

will artificially inflate the observational error covariance matrix $\mathbf{R} \approx (\sigma_m^2 + \sigma_b^2) \mathbf{I}$ and the errors will be incorrectly characterized in the observing system. As long as $\sigma_b < \sigma_m$, then $\mathbf{R} = \sigma_m^2 \mathbf{I}$ and the characterization of the errors will be appropriate.

2. Observing systems with more sites are generally less affected by site-specific systematic biases. This is because observing systems with a small number of sites rely heavily on those few sites. An observing system with many sites is less reliant on a single site and the site-specific systematic biases act more like additional noise in the observing system.
3. Systematic biases have a greater impact when estimating an area source than line and point sources. This is because an air mass sensitive to a line or point source will have a greater enhancement relative to the background compared to a diffuse area source; thus, there is a larger signal-to-noise ratio for these sources, and a systematic bias is less important.

During the day, model calculations of the planetary boundary layer height are more reliable leading to a temptation to omit the nighttime data from the analysis. However, emissions at night can be as much as 30 % of the total, and ignoring them makes estimates of urban emissions strongly dependent on prior assumptions. Our observing system would be unable to correct the misrepresented nighttime emissions of our atemporal prior without using nighttime observations. As a result, even our most optimistic observing system would have a systematic $\sim 50 \text{ tC h}^{-1}$ error ($\sim 30 \%$) in the estimated area source emissions due to the misrepresented nighttime emissions.

6.2 Potential cost trade-offs

We consider two potential observing systems:

1. “Network A” ($n_s = 25$, $\sigma_m = 1 \text{ ppm}$): a dense network with moderate-precision instruments. This network is similar to BEACO₂N, described in Sect. 3. We assume a cost of USD 5000 per instrument, giving a total cost of USD 125 000. This network is shown as a purple star in the left column of Fig. 4.
2. “Network B” ($n_s = 3$, $\sigma_m = 0.1 \text{ ppm}$): a sparse network with high-precision instruments. This network uses cavity ring-down instruments. We assume a cost of USD 50 000 per instrument, giving a total cost of USD 150 000. This network is shown as a green star in the left column of Fig. 4.

We note that the assumed mismatch error for these two potential observing systems is defined as the instrument error and assumes there is no contribution from model or transport errors.

The cost for these two networks is comparable. From Fig. 4, we find that the sparse Network B is site-limited in all cases, whereas the dense Network A is in the noise-limited regime. Further, we find that the dense Network A has less error in the estimate of all source types in San Francisco’s East Bay. Networks sitting on the ridge line are at the optimal balance between precision and number of sites.

6.3 The relationship between network density and transport error

In this work we have treated transport error and the number of measurement sites as independent. However, in practice, there would be a relationship between the transport error and measurement network density. This can be understood with a thought experiment using two different observing systems to estimate emissions: a sparse network with a single site and an infinitely dense network (sites at each grid cell in our domain). Estimating emissions with the sparse network would require us to simulate the atmospheric transport with high fidelity if we are to reliably say anything about emissions upwind of our site. This is especially true for point sources. Any errors in the simulated atmospheric transport would adversely impact the estimated emissions, whereas the infinitely dense network could potentially neglect atmospheric transport and use data from only the local grid cell to estimate emissions. This is because the differential signal at each site would be largely governed by the local emissions. Explicitly quantifying this relationship between transport error and measurement network density should be the focus of future work.

7 Conclusions

Understanding the factors that govern our ability to estimate urban greenhouse gas emissions are crucial to improving an observing system and reducing the uncertainty in emission estimates. Here we have quantitatively mapped the errors in CO₂ emission estimates from different observing systems for three different types of sources in California’s Bay Area: area sources, line sources, and point sources. Our results show that different observing systems may fall into noise or site-limited regimes where reducing the uncertainty in the estimated emissions is governed by a single factor; these regimes differ for the source types. Identifying the regime an observing system is in will help inform future improvements to the observing system. A number of prior urban CO₂ experiments have defined as a goal, the understanding of emissions to less than 10 % (e.g., Kort et al., 2013; Wu et al., 2016). We find that a BEACO₂N-like network could achieve this accuracy and precision with 1 week of observations if the dominant source of error is instrument precision. This conclusion may motivate a re-examining of the conventional instrument

quality-oriented design of CO₂ observing systems, according to the stated goal of a given network.

The Supplement related to this article is available online at doi:10.5194/acp-16-13465-2016-supplement.

Acknowledgements. This work was supported by a Department of Energy (DOE) Computational Science Graduate Fellowship (CSGF) to Alexander J. Turner, a National Science Foundation (NSF) Grant 1035050 to Ronald C. Cohen, and a Bay Area Air Quality Management District (BAAQMD) Grant 2013.145 to Ronald C. Cohen. Alexis A. Shusterman was supported by a National Science Foundation Graduate Research Fellowship. This research used resources of the National Energy Research Scientific Computing Center, which is supported by the Office of Science of the US Department of Energy under Contract No. DE-AC02-05CH11231. We thank M. Sulprizio (Harvard University) for gridding the US Census population data and the UC Berkeley Academic Computing center for access to computing resources.

Edited by: T. Butler

Reviewed by: two anonymous referees

References

- Bastien, L. A., McDonald, B. C., Brown, N. J., and Harley, R. A.: High-resolution mapping of sources contributing to urban air pollution using adjoint sensitivity analysis: benzene and diesel black carbon, *Environ. Sci. Technol.*, 49, 7276–7284, doi:10.1021/acs.est.5b00686, 2015.
- Bréon, F. M., Broquet, G., Puygrenier, V., Chevallier, F., Xueref-Remy, I., Ramonet, M., Dieudonné, E., Lopez, M., Schmidt, M., Perrussel, O., and Ciais, P.: An attempt at estimating Paris area CO₂ emissions from atmospheric concentration measurements, *Atmos. Chem. Phys.*, 15, 1707–1724, doi:10.5194/acp-15-1707-2015, 2015.
- Deschênes, O. and Greenstone, M.: Climate Change, Mortality, and Adaptation: Evidence from Annual Fluctuations in Weather in the US, *American Economic Journal: Applied Economics*, 3, 152–185, doi:10.1257/app.3.4.152, 2011.
- European Commission: Emission Database for Global Atmospheric Research (EDGAR), release version 4.2, Tech. rep., Joint Research Centre (JRC)/Netherlands Environmental Assessment Agency (PBL), 2011.
- Gately, C. K., Hutyra, L. R., Wing, I. S., and Brondfield, M. N.: A bottom up approach to on-road CO₂ emissions estimates: improved spatial accuracy and applications for regional planning, *Environ. Sci. Technol.*, 47, 2423–30, doi:10.1021/es304238v, 2013.
- Gately, C. K., Hutyra, L. R., and Sue Wing, I.: Cities, traffic, and CO₂: A multidecadal assessment of trends, drivers, and scaling relationships, *P. Natl. Acad. Sci. USA*, 112, 4999–5004, doi:10.1073/pnas.1421723112, 2015.
- Gratani, L. and Varone, L.: Daily and seasonal variation of CO₂ in the city of Rome in relationship with the traffic volume, *Atmos. Environ.*, 39, 2619–2624, doi:10.1016/j.atmosenv.2005.01.013, 2005.
- Gurney, K. R., Mendoza, D. L., Zhou, Y., Fischer, M. L., Miller, C. C., Geethakumar, S., and de la Rue du Can, S.: High resolution fossil fuel combustion CO₂ emission fluxes for the United States, *Environ. Sci. Technol.*, 43, 5535–5541, 2009.
- Gurney, K. R., Razlivanov, I., Song, Y., Zhou, Y., Benes, B., and Abdul-Massih, M.: Quantification of fossil fuel CO₂ emissions on the building/street scale for a large U.S. city, *Environ. Sci. Technol.*, 46, 12194–12202, doi:10.1021/es3011282, 2012.
- Hutyra, L. R., Duren, R., Gurney, K. R., Grimm, N., Kort, E. A., Larson, E., and Shrestha, G.: Urbanization and the carbon cycle: Current capabilities and research outlook from the natural sciences perspective, *Earth's Future*, 2, 473–495, doi:10.1002/2014ef000255, 2014.
- IPCC: Climate Change 2013: The Physical Science Basis. Contribution of Working Group I to the Fifth Assessment Report of the Intergovernmental Panel on Climate Change, Tech. rep., New York, NY, USA, 2013.
- Kort, E. A., Angevine, W. M., Duren, R., and Miller, C. E.: Surface observations for monitoring urban fossil fuel CO₂ emissions: Minimum site location requirements for the Los Angeles megacity, *J. Geophys. Res.-Atmos.*, 118, 1577–1584, doi:10.1002/jgrd.50135, 2013.
- Lauvaux, T., Miles, N. L., Richardson, S. J., Deng, A., Stauffer, D. R., Davis, K. J., Jacobson, G., Rella, C., Calonder, G.-P., and DeCola, P. L.: Urban Emissions of CO₂ from Davos, Switzerland: The First Real-Time Monitoring System Using an Atmospheric Inversion Technique, *J. Appl. Meteorol. Clim.*, 52, 2654–2668, doi:10.1175/jamc-d-13-038.1, 2013.
- Lin, J. C., Gerbig, C., Wofsy, S. C., Andrews, A. E., Daube, B. C., Davis, K. J., and Grainger, C. A.: A near-field tool for simulating the upstream influence of atmospheric observations: The Stochastic Time-Inverted Lagrangian Transport (STILT) model, *J. Geophys. Res.-Atmos.*, 108, ACH2-1–ACH2-17, doi:10.1029/2002jd003161, 2003.
- Mangat, T. S., Claire, S. J., Dinh, T. M., Fanai, A. K., Nguyen, M. H., and Schultz, S. A.: Source inventory of Bay Area greenhouse gas emissions, Tech. rep., Bay Area Air Quality Management District, San Francisco, CA, USA, 2010.
- McDonald, B. C., McBride, Z. C., Martin, E. W., and Harley, R. A.: High-resolution mapping of motor vehicle carbon dioxide emissions, *J. Geophys. Res.-Atmos.*, 119, 5283–5298, doi:10.1002/2013jd021219, 2014.
- McKain, K., Wofsy, S. C., Nehr Korn, T., Eluszkiewicz, J., Ehleringer, J. R., and Stephens, B. B.: Assessment of ground-based atmospheric observations for verification of greenhouse gas emissions from an urban region, *P. Natl. Acad. Sci. USA*, 109, 8423–8428, doi:10.1073/pnas.1116645109, 2012.
- Meirink, J. F., Bergamaschi, P., and Krol, M. C.: Four-dimensional variational data assimilation for inverse modelling of atmospheric methane emissions: method and comparison with synthesis inversion, *Atmos. Chem. Phys.*, 8, 6341–6353, doi:10.5194/acp-8-6341-2008, 2008.
- Nassar, R., Napier-Linton, L., Gurney, K. R., Andres, R. J., Oda, T., Vogel, F. R., and Deng, F.: Improving the temporal and spatial distribution of CO₂ emissions from global fossil fuel

- emission data sets, *J. Geophys. Res.-Atmos.*, 118, 917–933, doi:10.1029/2012jd018196, 2013.
- Nehrkorn, T., Eluszkiewicz, J., Wofsy, S. C., Lin, J. C., Gerbig, C., Longo, M., and Freitas, S.: Coupled weather research and forecasting–stochastic time-inverted lagrangian transport (WRF–STILT) model, *Meteorol. Atmos. Phys.*, 107, 51–64, doi:10.1007/s00703-010-0068-x, 2010.
- Newman, S., Jeong, S., Fischer, M. L., Xu, X., Haman, C. L., Lefer, B., Alvarez, S., Rappenglueck, B., Kort, E. A., Andrews, A. E., Peischl, J., Gurney, K. R., Miller, C. E., and Yung, Y. L.: Diurnal tracking of anthropogenic CO₂ emissions in the Los Angeles basin megacity during spring 2010, *Atmos. Chem. Phys.*, 13, 4359–4372, doi:10.5194/acp-13-4359-2013, 2013.
- Oda, T. and Maksyutov, S.: A very high-resolution (1 km × 1 km) global fossil fuel CO₂ emission inventory derived using a point source database and satellite observations of nighttime lights, *Atmos. Chem. Phys.*, 11, 543–556, doi:10.5194/acp-11-543-2011, 2011.
- Peters, W., Jacobson, A. R., Sweeney, C., Andrews, A. E., Conway, T. J., Masarie, K., Miller, J. B., Bruhwiler, L. M., Petron, G., Hirsch, A. I., Worthy, D. E., van der Werf, G. R., Randerson, J. T., Wennberg, P. O., Krol, M. C., and Tans, P. P.: An atmospheric perspective on North American carbon dioxide exchange: CarbonTracker, *P. Natl. Acad. Sci. USA*, 104, 18925–18930, doi:10.1073/pnas.0708986104, 2007.
- Rigby, M., Toumi, R., Fisher, R., Lowry, D., and Nisbet, E. G.: First continuous measurements of CO₂ mixing ratio in central London using a compact diffusion probe, *Atmos. Environ.*, 42, 8943–8953, doi:10.1016/j.atmosenv.2008.06.040, 2008.
- Rodgers, C. D.: *Inverse Methods for Atmospheric Sounding*, World Scientific, Singapore, 2000.
- Shusterman, A. A., Teige, V., Turner, A. J., Newman, C., Kim, J., and Cohen, R. C.: The BERkeley Atmospheric CO₂ Observation Network: initial evaluation, *Atmos. Chem. Phys. Discuss.*, doi:10.5194/acp-2016-530, in review, 2016.
- Singh, K., Jardak, M., Sandu, A., Bowman, K., Lee, M., and Jones, D.: Construction of non-diagonal background error covariance matrices for global chemical data assimilation, *Geosci. Model Dev.*, 4, 299–316, doi:10.5194/gmd-4-299-2011, 2011.
- Turnbull, J. C., Sweeney, C., Karion, A., Newberger, T., Lehman, S. J., Tans, P. P., Davis, K. J., Lauvaux, T., Miles, N. L., Richardson, S. J., Cambaliza, M. O., Shepson, P. B., Gurney, K., Patarasuk, R., and Razlivanov, I.: Toward quantification and source sector identification of fossil fuel CO₂ emissions from an urban area: Results from the INFLUX experiment, *J. Geophys. Res.-Atmos.*, 120, 292–312, doi:10.1002/2014JD022555, 2015.
- US EIA: *Emissions of Greenhouse Gases in the U.S.*, Tech. rep., US Energy Information Administration, 2015.
- Wu, L., Broquet, G., Ciais, P., Bellassen, V., Vogel, F., Chevalier, F., Xueref-Remy, I., and Wang, Y.: What would dense atmospheric observation networks bring to the quantification of city CO₂ emissions?, *Atmos. Chem. Phys.*, 16, 7743–7771, doi:10.5194/acp-16-7743-2016, 2016.
- Yadav, V. and Michalak, A. M.: Improving computational efficiency in large linear inverse problems: an example from carbon dioxide flux estimation, *Geosci. Model Dev.*, 6, 583–590, doi:10.5194/gmd-6-583-2013, 2013.